**Atmospheric
Chemistry
and Physics
Discussions**

Modelling multi-phase halogen chemistry in the coastal marine boundary layer: investigation of the relative importance of local chemistry vs. long-range transport

D. Lowe[1], J. Ryder[1,2], R. Leigh[3,*], J. R. Dorsey[1], and G. McFiggans[1]

[1]Centre for Atmospheric Sciences, School of Earth, Atmospheric and Environmental Sciences, University of Manchester, Manchester, M13 9PL, UK
[2]Centre for Ecology and Hydrology, Midlothian, EH26 0QB, UK
[3]Department of Physics and Astronomy, University of Leicester, Leicester, LE1 7RH, UK
[*]now at: Crichton Carbon Centre, Crichton University Campus, Dumfries, DG1 4ZL, UK

Correspondence to: D. Lowe (douglas.lowe@manchester.ac.uk)

Abstract

Measurements of significant concentrations of IO, I_2 and BrO in a semi-polluted coast environment at Roscoff, in North-West France, have been made as part of the Reactive Halogens in the Marine Boundary Layer (RHaMBLe) campaign undertaken in September 2006. We use a one-dimensional column model, with idealised I_2 emissions predicted using macroalgael maps and tidal data from the littoral area surrounding Roscoff, to investigate the probable causes for these observations. The coupled microphysical and chemical aerosol model simulates mixed-phase halogen chemistry using two separate particle modes, seasalt and non-seasalt, each comprising of eight size-sections. This work confirms the finding of a previous study that the BrO measurements are most likely caused by unknown, local sources. We find that the remote observations of IO and I_2 are best replicated using the I_2 recycling mechanism suggested by previous studies, but that such a mechanism is not wholly necessary. However we suggest that focussed observations of the changes in NO_x and NO_y concentrations, as well as changes in the nitrate fraction of the non-seasalt aerosol mode, in the presence of I_2 bursts could be used to determine the atmospheric relevance of the predicted I_2 recycling mechanism.

1 Introduction

Research into tropospheric iodine and bromine radical species has been driven by their potential to influence important atmospheric chemical processes. These include changing the oxidative capacity of the atmosphere via destruction of ozone in catalytic cycles (Davis et al., 1996; Read et al., 2008), and by altering the partitioning of NO_x and HO_x (McFiggans et al., 2000; Platt and Hönninger, 2003; Bloss et al., 2005); and the formation and growth of new particles (Hoffmann et al., 2001; Odowd et al., 2002; McFiggans et al., 2004). Field measurements in the coastal marine boundary layer (MBL) have identified both bromine- and iodine-containing inorganic species (e.g., Al-

lan et al., 2000; Saiz-Lopez and Plane, 2004; Saiz-Lopez et al., 2004; Peters et al., 2005). The main source of reactive bromine species in the MBL is likely to be sea-salt aerosol (Vogt et al., 1996; Sander et al., 2003). In addition the direct emission of organohalogens and molecular iodine by macroalgae will also contribute significantly
5 to halogen loading in the coastal MBL (Carpenter et al., 1999; Palmer et al., 2005).

The Reactive Halogens in the Marine Boundary Layer (RHaMBLe) project at Roscoff, Brittany, was designed to investigate Marine Boundary Layer (MBL) chemistry in semi-polluted conditions. To investigate daytime tidal signature of iodine photochemistry and new particle bursts. Roscoff was chosen for its large tidal range and extensive,
10 well mapped, macroalgal beds. Which indicated a good likelihood of significant I_2 emissions. Measurements were conducted during September 2006. See McFiggans et al. (2010) for a detailed overview of the campaign.

Remote measurements of BrO, IO, OIO, I_2, NO_3, and O_3 were made using a Differential Optical Absorption Spectroscopy (DOAS) instrument (Mahajan et al., 2009a,b).
15 These measured high BrO and IO levels concurrently with high levels of NO_3. In-situ measurements of IO were made with a Laser Induced Fluorescence (LIF) instrument (Whalley et al., 2007) and a open-path cavity ring-down spectroscopy (CRDS) instrument (Wada et al., 2007). NO_2 was measured in-situ using a chemiluminesence NO instrument with photolytic NO_2 converter, as was O_3 using a standard UV absorption
20 instrument.

Measurements of I_2, IO, OIO, BrO and NO_2 to the north of Roscoff were made using long-path Differential Optical Absorption Spectroscopy (LP-DOAS) (Mahajan et al., 2009a,b). The light path of the LP-DOAS instrument extended out to the North-West, with an optical path length of 6.7 km, crossing the inter-tidal zone at a height of
25 7–12 m above mean sea level. Measurements of iodine species showed a clear tidal relationship, high mixing ratios at low tide and vice versa. During the day the maximum mixing ratios measured for I_2 and IO were 25.9±3.1 pptv (measured on 19 September 2006) and 10.1±0.7 pptv (9 September 2006), respectively (Mahajan et al., 2009b). No daytime measurements of OIO were above the LP-DOAS detection limit (4 pptv). BrO

measurements did not exhibit a tidal relationship; the maximum mixing ratio measured by the LP-DOAS was 7.5±1.0 pptv (Mahajan et al., 2009a).

Three previous modelling studies have been conducted to examine iodine and bromine chemistry at Roscoff. Mahajan et al. (2009b) used a one-dimensional gas-phase photochemistry and transport model (THAMO) to investigate the LP-DOAS I_2 and IO measurements. An I_2 injection of rate of 1×10^{-11} molecules cm^{-2} s^{-1} for 200 s was used to simulate a homogeneous macroalgal bed of around 1 km width. The peak I_2 and IO measured concentrations were multiplied by a factor 3.4 to account for the heterogeneity of I_2 sources below the LP-DOAS lightpath (the lightpath is 3.4 km long). They also calculated the ratios of the measured I_2:IO concentrations, obtaining an average ratio of 3.8. Mahajan et al. (2009b) found that the modelled I_2:IO ratio at the LP-DOAS measurement height ($\approx$10 m) was too low without a reaction for recycling I_2 – for this they used the reaction:

$$I + IONO_2 \rightarrow I_2 \tag{1}$$

with a rate of 5.5×10^{-11} cm^3 molecules^{-1} s^{-1} (Kaltsoyannis and Plane, 2008).

Leigh et al. (2009) used footprint concentration modelling to investigate the local macroalgal emission contributions to the remote and in-situ I_2 measurements. Bathymetry and speciated macroalgal distribution information is mapped onto a two dimensional flat grid, each cell of which was $0.0005° \times 0.0005°$ (approximately 36.7 m longitudinally $\times$ 55.6 m latitudinally). Tidal and meteorological data was applied at a one minute resolution for the period of the campaign. Emissions were calculated from seaweed species and exposure time, with emissions decreasing with time from first exposure (Ball et al., 2009). Emission footprints were calculated for windspeed and tidal height, rotated due to wind direction, and then applied to the emissions grid to calculate concentration footprints (assuming emission into a 15 cm thick layer). Chemistry was not included, however photolytic destruction of I_2 was considered, with travel time across the footprint estimated from the windspeed. A simple recycling parameter was included, simulating the reforming of a certain proportion of the photo-dissociated I_2.

It was found that reasonable correlations between modelled concentrations and data from the LP-DOAS and in-situ BBCEAS instruments could only be obtained during the day through the implementation of a simulated recycling scheme such that I_2 is maintained at the level it would have with approximately 95% slower photolysis, suggesting that either unmodelled local emissions, or a significant missing recycling or source component.

Mahajan et al. (2009a) used a gas-phase photochemical box model to investigate the conditions in which more than 5 ppt of BrO can be generated in a mildly polluted environment. The model was initialised with 2 ppb NO_2 and 100 ppt Br_2, and run for 20 h. Around 6 h in the BrO mixing ratio reached a maximum of $\approx$5.5 ppt, with the majority of bromine as $BrONO_2$ ($\approx$110 ppt). They examined a number of scenarios – eliminating sea-salt and biogenic bromine compounds as possible sources, instead suggesting that an unknown local source was the most likely cause.

The aim of this study is to investigate the importance of vertical transport and chemical mixing for the observations of concurrent high halogen oxide and NO_2 levels at a semi-polluted coastal location. Towards this end a simple one-dimensional column model has been developed treating the evolution of the gas- and condensed-phase composition driven by vertical turbulent mixing and a highly-detailed representation of the multi-phase photochemistry. Although a reasonable multi-day simulation of the key processes has been used to ensure the model approaches the coastline with representative gaseous and condensed phase component loadings, the study focuses on detailed prediction of the coupled chemistry, microphysics and vertical transport that occurs as the emissions from the coastal zone mix into the background air. This then allows quantitative assessment of our understanding of the processes by comparison of the simulated behaviour with in situ measurements.

2 Model description

The one-dimensional column model used in this study is built around the box-model MANIC (Microphysical Aerosol Numerical model Incorporating Chemistry) (Lowe et al., 2009), which explicitly links aerosol chemistry and microphysics. A simple eddy diffusivity model is used to simulate vertical transport, driven by turbulence profiles generated off-line (no feedbacks between aerosols and heat fluxes are considered). Operator splitting is used, with microphysical and chemical processes being calculated in a separate step for each 1-D column cell, followed by a vertical transport step for the whole column. Fluxes of gases and seasalt aerosol particles from the sea surface are considered, as well as entrainment of gases from the free troposphere – the important processes which are dealt with in the model are shown in Fig. 1.

2.1 Microphysics and chemistry

The chemistry scheme used is based on that of Pechtl et al. (2006), with the updates detailed in Lowe et al. (2009). Non-ideality of the major ions in the condensed phase (H^+-Na^+-NH_4^+-HSO_4^--SO_4^{2-}-NO_3^--Cl^-) is treated using PD-FiTE (Topping et al., 2009). I_xO_y chemistry has been included (Table 1, based on the scheme of Saiz-Lopez et al., 2008), to simulate the irreversible conversion of reactive iodine to inert species often viewed as the most likely candidates for new particle formation. While such postulations that I_xO_y species are involved in the nucleation of new particles, we do not treat this process, the nucleation and growth of ultrafine particles being beyond the scope of the current paper. It is not expected that a newly formed nucleation mode of particles will significantly influence the conclusions of the current work. Photolysis rates are calculated from actinic fluxes, which were measured at Roscoff during the RHaMBLe campaign using a Metcon spectral radiometer (Edwards and Monks, 2003).

Further simplification of the treatment of aerosol is provided by not considering coagulation or any possible phase separation, nor including organic aerosol components. The condensed-phase is split into two separate populations: seasalt and non-seasalt,

each of which comprises 8 size-sections. This distinction is purely based on the aerosol origin – the same chemical reactions and microphysical processes are applied to each population during the model run. Aerosol dry deposition is treated using the resistance model of Slinn and Slinn (1980); wet deposition is not considered.

Seasalt aerosol particles are predominately generated by bubble bursting during whitecap formation caused by surface winds. Monahan et al. (1986) used observational and laboratory data of particle production for droplets between 0.4–20 µm radii to parameterise this process. Their scheme, however, over-predicted production of seasalt particles with radii less than 0.2 µm when compared with field measurements (O'Dowd et al., 1997). Gong (2003) introduced a new parameter, Θ, to control the shape of the sub-micron size distributions, extending the applicability of the scheme down to dry radii of 0.02 µm. The particle number flux, F_N, is given as

$$\frac{dF_N}{dr_{80}} = 1.373 u_{10}^{3.41} r_{80}^{-A} (1 + 0.057 r_{80}^{3.45}) \times 10^{1.607 e^{-B^2}} \tag{2}$$

where $A = 4.7(1 + \Theta r_{80})^{-0.017 r_{80}^{-1.44}}$, $B = \frac{0.433 - \log r_{80}}{0.433}$, u_{10} is the wind speed at a height of 10 m above the ground, r_{80} is the particle radius at RH=80% and Θ=30 (after Gong, 2003).

2.2 1-D vertical transport scheme

Vertical transport is determined by the diffusion equation:

$$\frac{\delta c}{\delta t} = \frac{\delta}{\delta z}\left(K_e \frac{\delta c}{\delta z}\right) + \frac{\delta(v_T c)}{\delta z} \tag{3}$$

where c is concentration (either particles cm^{-3} or molecules cm^{-3}), t is time (s), z is height (m), K_e is the eddy diffusivity (m^2 s^{-1}), and v_T is the terminal settling velocity (m s^{-1}). For gas-phase transport we assume that v_T=0, while for particulate transport it is calculated using the scheme from Hoppel et al. (2005). Equation (3) is discretised

following the formulation of ApSimon et al. (1994), enabling the use of a non-uniform grid. A fourth-order Runge-Kutta method is used to integrate the diffusion equation (Press et al., 1989), taking timesteps of 0.05 s. K_e is proscribed in the model input files, the vertical profiles used for this case study are described below.

3 Case study setup

3.1 1-D column layout and meteorology

The 1-D column is set to 1000 m height, divided into 25 levels. The lowest 25 m of the column is split into 6 levels, with boundaries at 1, 3, 6, 10 and 15 m.

Air pressure is assumed to decrease linearly with height (with a pressure of 1020 mbar at the ground surface, and a lapse rate of 0.113 mbar m^{-1}). The temperature profile follows a simple diurnal profile. During the day the ground surface temperature is 290 K, decreasing at the dry adiabatic lapse rate (9.76×10^{-3} K m^{-1}) to the top of the column. At night the ground surface temperature is 284 K, decreasing at the dry adiabatic lapse rate up to a height of 300 m. Above this height air temperature increases again, to reach 282 K at the top of the column. Relative humidity is calculated on-line from pressure, temperature and the H$_2$O mixing ratio.

A simplified eddy diffusivity profile is calculated off-line according to the parameterisation of Myrup and Ranzieri (1976), assuming that the atmospheric conditions are neutral:

$$K_e = \begin{cases} \kappa u_* z \,, & z/z_i < 0.1 \\ \kappa u_* z (1.1 - z/z_i) \,, & 0.1 \leq z/z_i \leq 1.1 \\ 0 \,, & z/z_i > 1.1 \end{cases} \tag{4}$$

where z is height of column-section edge, z_i is the characteristic vertical length-scale (in this instance the mixed-layer depth), κ is the von Karman constant. u_* is the friction velocity, calculated using the ACASA model (described in Pyles et al., 2003, 2004) for

the lowest 70 m of the model column. Above 70 m we assume that u_* is constant (equal to the value at 70 m). z_i is set to 300 m during the night, and is set to 900 m during the day. Dawn is at 06:30 LT, dusk at 17:30 LT, and the transition from day to night conditions is linear over the hour following dawn and dusk.

Photolysis rates are calculated from solar irradiance measured on the day of 23 September 2006 under close to clear sky conditions.

Included in the supplementary material are the column section heights; pressure, temperature and eddy diffusivity vertical profiles; and a plot of the solar irradiance.

3.2 Trajectory configuration

The model is given a 59 h spin-up period before the final hour approaching the coastline, to allow the model chemistry to allow more realistic and stable component loadings on the approach to the coastline (in comparison to the rather simplistic initial conditions). One particular background scenario has been chosen to provide the most frequently observed polluted marine conditions encountered during the RHaMBLe field project. This entails running a background marine airmass across the UK and then the Channel before finally arriving at Roscoff (an example trajectory of this type is included in the supplementary material).

The first 48 h of the model run (starting at midnight) are across a clean marine environment, representative of conditions above the Atlantic. The gas-phases of all levels in the vertical column are initialised with the mixing ratios given in Table 2 (fixed species are constant at the given mixing ratios throughout the whole vertical column and model run). The model is initialised with two aerosol modes – one seasalt, the other non-seasalt – with initial distributions which are also consistent throughout the whole column. The seasalt initial distribution is a pseudo-lognormal, bi-modal, distribution (Porter and Clarke, 1997), which is linearly scaled to yield a dry mass of 15 μg; m_{air}^{-3} (after Toyota et al., 2001). The dry composition used is 99.4317% NaCl, 0.1491498% NaBr, 1.372178×10^{-5}% NaI, 4.812565×10^{-5}% NaIO$_3$, and 0.4176193%

NaHCO$_3$. The non-seasalt initial distribution is given in Table 5. The initial dry composition of the non-seasalt mode is 46% NH$_4$NO$_3$, 18% NH$_4$HSO$_4$ and 36% (NH$_4$)$_2$SO$_4$.

During this ocean leg seasalt aerosol is emitted using Eq. (2) and a wind speed of 5.25 m s^{-1}. The composition of this fresh aerosol is the same as that for the initial seasalt distribution, given above. Gas emissions from the ocean surface are given in Table 3, and the gas deposition rates used throughout the whole model run are given in Table 4.

Following the Atlantic leg the column is run across a polluted land environment for 6 h, representing passage over the UK. Seasalt emissions are switched off, and the land-based emissions given in Table 3 are used. These source terms were chosen to ensure the modelled NO$_x$ concentrations were within the range of NO$_x$ concentrations measured at Roscoff during the RHaMBLe campaign.

A 5 h run across a marine environment is made again, simulating the air column crossing the English Channel. Seasalt aerosol and gas-phase emissions are the same as for the Atlantic leg. A snapshot of the gas- and condensed-phase mixing ratios throughout the entire column is taken at the end of the Channel leg. This is used to initialise the 1 h Roscoff runs which are discussed in this paper.

Plots of prognostic variables for the spin-up period have been included in the supplementary material.

3.3 Roscoff leg settings

The model study presented in this paper consists of the last hour of the run, leading into Roscoff. Two scenarios are considered: high-tide, in which the model runs over the sea for the whole hour (as for the Channel leg); and low-tide, which is part sea and part intertidal exposed shoreline. The exposed intertidal section has no aerosol or gas emissions (unlike the sea or UK sections) other than localised I$_2$ emissions from macroalgae generated by a footprint emissions model for the measurement site at Roscoff (Leigh et al., 2009). This combines tidal data, macroalgael maps, and wind speed and direction data taken at the in-situ measurement site during the RHaMBLe

campaign.

The Leigh et al. (2009) model has been adapted for this study. For each 1-min model timestep, the emission footprint applied was reduced to the width of a single model cell (55 m), and extended upwind from the measurement site to the calculated sea edge. I_2 emissions within this footprint were characterised by transport time to site, assuming a constant wind speed and direction along the trajectory. I_2 emissions were calculated for every 30 s section of the trajectory.

For this study the highest total I_2 emission scenario has been used as a case study. This occurred on the 10 September 2006, arriving at Roscoff at 12:30 p.m. (Fig. 2). There are three I_2 bursts. The first is from 11.7375 to 11.7875 h (lasting 3 min), with a peak emission rate of 8.26×10^9 molecules cm^{-2} s^{-1}. The second and third bursts are shorter, 1 and 1.25 min long, respectively, and starting at 11.9292 and 11.9792 h. The peak emission rates are also much lower, 1.04×10^9 and 1.95×10^8 molecules cm^{-2} s^{-1}, respectively.

4 Results and discussion

Here, the gas- and condensed-phase chemical behaviour in the last hour of the model run approaching Roscoff is examined in detail. The model reaches Roscoff at midday (12:00 LT). The major gas- and condensed-phase species for the base case, low tide, model run are plotted below (Figs. 3, 5, 6, 7 and 8). Data from the other runs will be included where relevant to the discussion, however plots of major chemical species data from all model runs are also included in the supplementary material.

4.1 Low tide base case

At the start of the Roscoff leg the air column is still over the sea. Strong vertical gradients in the mixing ratios of gas-phase halogen species and pollutants, such as HNO$_3$ (Fig. 3) are observed. These result from the source of fresh seasalt, which main-

tains higher seasalt aerosol volumes in the lowest 10–20 m of the column (Fig. 4). The largest seasalt particles experience rapid turnover at the base of the column, producing a strong gradient in composition across vertical- and size-space for seasalt particles (Figs. 5 and 6). The pH of the largest, and vertically lowest, seasalt particles is around 9–10, as compared to a pH of 5–4 for the smallest, and highest vertically, particles. Likewise the Br^- content of the largest particles at the base of the column is close to that of fresh seasalt, while at a height of 650 m the mole fraction of Br^- in the smallest particles has been reduced by a factor of 100. Cl^- remains relatively undepleted in the largest seasalt particles (the molar ratio of Cl^- to Na^+ is ≤ 0.8 for the three largest size bins, indicating a loss of less than 20% of the initial Cl^- content of these particles). The Cl^- content of the smaller seasalt particles is more depleted, and the pollutant (NO_3^- and sulphate) content of these particles is much higher, due to their higher surface area to volume ratio (and so higher gas-aerosol transfer rate compared with total mass). The non-seasalt mode exhibits marked vertical-dependence, but little or no size-dependence, in composition (Figs. 7 and 8). pH decreases with height, as the relative humidity decreases. The $HSO_4^-:SO_4^{2-}$ ratio changes with pH. NO_3^- and Cl^- content increases with height. Br^- and I^- content is minor at all heights.

At 11.43 h the air column crosses from the sea to the beach. This stops the injection of fresh seasalt into the model column, halting this source of halogens, and leading to a reduction in seasalt aerosol volume and surface area (Fig. 4) due to sedimentation. The effects of stopping this seasalt source term can been seen almost immediately in the gas-phase (Fig. 3). The mixing ratios of halogen species in the lowest few sections relax back towards the mixing ratios observed higher in the model column; as do the mixing ratios of HNO_3 and O_3. The increase in HNO_3 mixing ratio is the result of the decrease in seasalt aerosol mass, and the rapid acidification of the largest seasalt particles (Fig. 5), in the lowest sections of the column; diffusive mixing then reduces the vertical gradient in mixing ratio. Chlorine and bromine species reactions to the switching off the seasalt source term are mixed. The mixing ratios of Br, BrCl, BrO, and HOBr drop, mostly due to vertical mixing bringing these species closer to the

Title Page

Abstract | Introduction

Conclusions | References

Tables | Figures

|◄ | ►|

◄ | ►

Back | Close

Full Screen / Esc

Printer-friendly Version

Interactive Discussion

mixing ratios of the main body of the column. Conversely, the mixing ratios of $BrONO_2$, HBr, $ClONO_2$, HCl, and ClO increase. This is likely to be due to a reduction in aerosol processing (due to loss of Cl^- and Br^-, and reduction in surface area) for the halogen nitrates, while the increases in the chlorine species will also be due to the release of chlorine from the largest seasalt particles as they become much more acidified (the drop in pH is matched by a reduction in the $Cl^-:Na^+$ ratio from ≈ 0.95 to ≈ 0.8).

At 11.74, 11.93 and 11.98 h there are I_2 bursts, simulating iodine emissions by macroalgae (Fig. 2). In the lowest level (0–1 m) the I_2 mixing ratios reach a maximum of 2000 pmol mol^{-1} during the first burst (Fig. 9). This maximum drops off sharply with height, down to only 470 pmol mol^{-1} in the next level (1–3 m), and 20 pmol mol^{-1} by the fifth level (10–15 m). The mixing ratio of I_2 quickly becomes negligible once it's source term is switched off again (as we would expect without any recycling processes). The reactive iodine species, I, IO, and OIO are almost as short-lived (Figs. 3 and 9), although their vertical gradients are not so drastic. Most iodine from the bursts becomes $IONO_2$ and I_xO_y, which reach maxima of 1400 and 920 pmol mol^{-1} in the lowest level (and 1200 and 670 in the second level), respectively. Vertical mixing leads to the dispersion of these species fairly evenly over the lowest 60–100 m of the column, at mixing ratios of 100–50 pmol mol^{-1}.

The LP-DOAS lightpath runs at an average of 8–10 m above mean sea level. Comparisons with the model column should therefore focus on levels 3 and 4 (6–10 m and 10–15 m), although variations in topography along the lightpath means that I_2 sources could be anything from 2–3 m to 15–20 m below the lightpath. The model IO mixing ratios peak between 70–40 pmol mol^{-1} in these levels; 7–4 times the maximum measured IO mixing ratios. The model I_2 mixing ratios peak between 160–50 pmol mol^{-1} in these levels; 6–2 times the maximum measured I_2 mixing ratios. OIO was not measured above the detection limit during the day, however the modelled OIO mixing ratios peak between 20–10 pmol mol^{-1} in these levels, only 5–2.5 times the detection limit (4 pptv). The LP-DOAS measurements are averaged over a path of 6.7 km, heterogeneity in the distribution of species across the path could mean that local maxima

are much higher than the measured levels. The differences between the modelled and measured mixing ratios could be explained by this heterogeneity, however the I_2:IO ratio during the I_2 bursts is only 2.5–2 at these levels, much less than the average ratio of 3.8 that Mahajan et al. (2009b) calculated from the LP-DOAS measurements. A ratio of 4 is reached at a height of 1–3 m above the I_2 source, at which the I_2 and IO are 20–30 times higher than the measurements, suggesting that strong, but spatially limited, I_2 sources could reproduce the LP-DOAS measurements if only a couple of metres below the lightpath.

Mixing ratios of reactive chlorine and bromine species drop precipitously within the I_2 bursts, as they are converted to ICl and IBr by cross-reactions, before increasing equally markedly at the end of the bursts (Figs. 3 and 9). The increases in gas-phase mixing ratios are driven by the extraction of Cl^- and Br^- from the condensed phase, both from the seasalt mode (Fig. 5) and, less importantly, from the non-seasalt mode (Fig. 8), by iodine. The increase in gas-phase chlorine species is more marked than that of bromine species simply because there is a larger Cl^- reservoir in the seasalt mode (which is hardly reduced by the iodine burst).

The first iodine burst also leads to the destruction of around 20% of the O_3 in the lowest level, and consumes practically all HO_x as well as ≈ 1200 pmol mol^{-1} of NO_x. These perturbations are also short-lived, though, with mixing replacing the majority of the lost O_3 and NO_x. HO_x are increased after the burst, boosted by the decrease in NO_x levels (Fig. 3). The NO_3^- content of the non-seasalt mode increases during the Iodine bursts (Fig. 8), presumably driven by heterogeneous reactions of $IONO_2$ with the non-seasalt mode, although it should be noted that the NO_3^- of the seasalt mode does not increase at the same time (Fig. 6).

4.2 I_2 recycling

Mahajan et al. (2009b) reported an increase in NO_3 mixing ratios, to ≈ 10 ppt, when using the I_2 recycling reaction (Reaction 1). Without this reaction an increase in NO_3 is

observed in the current work, but only to $\approx 1 \, \text{pmol mol}^{-1}$ (Fig. 9). Reaction (1) has been included in the current model to examine the changes in iodine compound mixing ratios and to investigate other changes in the mixed-phase chemistry occur. This version of the model was used to simulate low tide at Roscoff, initialised from the same starting
5   mixing ratios as the base case Roscoff runs.

I_2 mixing ratios were found to be higher than the base case (reaching $2400 \, \text{pmol mol}^{-1}$ in the lowest level), and tail off more gently after the end of the I_2 burst. This increases IO, OIO, and I_xO_y mixing ratios (Fig. 10), while peak $IONO_2$ mixing ratios drastically decrease to $\approx 210 \, \text{pmol mol}^{-1}$ (see supplementary material).
10 At the column height of 6–15 m peak IO increases to 80–$50 \, \text{pmol mol}^{-1}$, peak I_2 to 340–$170 \, \text{pmol mol}^{-1}$, and peak OIO to 27–$16 \, \text{pmol mol}^{-1}$. I_2:IO ratios at this height increases to 4.2–3.3, which drops away to 2–1 after the I_2 burst. This fits well with the LP-DOAS measurements, as found by Mahajan et al. (2009b).

NO_3 increases to $\approx 10 \, \text{pmol mol}^{-1}$, consistent with the finding of Mahajan
15 et al. (2009b), and may be a measurable diagnostic for I_2 recycling in the ambient atmosphere. This increase changes the response of NO_2 mixing ratios to the I_2 burst, which dramatically increases by $500 \, \text{pmol mol}^{-1}$ during the burst, rather than decreasing by $100 \, \text{pmol mol}^{-1}$ as the basic model does (see supplementary material). The decrease in $IONO_2$ mixing ratios also reduces the depletion of Cl^- and
20 Br^- from the condensed-phase via heterogeneous reactions. The reduction of these heterogeneous reactions also decreases the accumulation of NO_3^- in the non-seasalt mode during the I_2 bursts. This reduces the peak NO_3^- dry mole fraction from 0.13 to 0.11 (Figs. 8 and 11), and so reduces the growth of the non-seasalt mode due to the uptake of nitrate (Figs. 4 and 11). Our model does not, however, deal with the con-
25 densation of I_xO_y species, the increase of which could compensate for this reduction in particle growth. However it should also be noted that nucleation, which is thought to be an appreciable sink of the I_xO_y species, is also not accounted for in the model.

4.3 Simulated BrO concentrations

BrO mixing ratios are very low throughout the model run at around 2–4×10^{-3} pmol mol^{-1}. Most measurements of daytime BrO made during the RHaM-BLe campaign were around 1–2 ppt with a maximum of 7 ppt (Mahajan et al., 2009a). In the base case simulation most gaseous bromine in the model is in the form of BrNO$_2$ (4.6–4.8 pmol mol^{-1}) and BrCl (1–1.2 pmol mol^{-1}), with the majority of the rest in BrONO$_2$ and HBr, at 0.12–0.2 and 0.07–0.16 pmol mol^{-1}, respectively (Fig. 3). The total bromine in the gas-phase ranges from 6.0–6.4 pmol mol^{-1}, having accumulated gradually over the Channel run as fresh seasalt comes into contact with polluted air (condensed-phase bromine content is 0.14 pmol mol^{-1} immediately above the sea-surface, dropping to 0.0002 pmol mol^{-1} with height, and when over the exposed intertidal region).

With an average daytime maximum BrO mixing ratio of only 3×10^{-3} pmol mol^{-1}, it is a factor of 1000 less than the BrO observations made at Roscoff. Mahajan et al. (2009a) observed that the measured BrO mixing ratios could be replicated in a polluted environment if there was a total bromine loading of 200 ppt, otherwise current chemistry schemes could not explain the BrO observations. They used a simple gas-phase box-model for this study, forced with an initial content of 100 ppt Br$_2$. To investigate what kind of bromine sources needed to replicate the BrO measurements three testcases were performed with Br$_2$ sources. The first two use a Br$_2$ source term from the sea of 3×10^{10} molecules cm^{-2} s^{-1} (which runs from the start of the Channel leg and across the sea-section of the Roscoff legs), one using the Roscoff high-tide scenario, the other the low-tide scenario. The third testcase is initialised using the same Channel leg as the original testcases, but has a constant Br$_2$ source term across the intertidal zone of 5×10^{10} molecules cm^{-2} s^{-1} (using the low-tide scenario only).

Ozone and bromine compound mixing ratios for the lowest 5 levels from each of the three model runs are shown in Fig. 12. Br$_2$ mixing ratios are, as would be expected, higher in the beach Br$_2$ source term scenario. BrO mixing ratios are, however,

very similar between the two different source terms, around 8–15 pmol mol^{-1} in the lowest level, and 2–4 pmol mol^{-1} between 8–15 m height. This is due to the build up of reservoir bromine compounds during the Channel leg with a sea Br_2 source term. The responses of Br_2, Br, and BrO to changes in the Br_2 source term are very rapid.
All other bromine compounds show a steady increase in mixing ratio with time (with a vertical gradient) when the Br_2 source is active, but then drop off when the source is switched off (as vertical mixing becomes the dominant process and brings their mixing ratios in line with the bulk of the vertical column). The majority of gas-phase bromine is still locked up in $BrNO_2$, which reaches 500 pmol mol^{-1} in the lowest level after 5.5 h of Br_2 emissions, and increases rapidly to 400 pmol mol^{-1} when the beach Br_2 source term is switched on.

The I_2 bursts have a very strong effect on the BrO mixing ratios, reducing BrO by 5 pmol mol^{-1} within the centre of the burst. The rapid response of BrO to changes in source term, as well as to changes in halogen chemistry, suggests that a very localised reactive bromine source is needed to explain the observations.

5 Conclusions

LP-DOAS IO and OIO observations (or lack thereof) are likely the result of localised emissions from macroalgae, which are diluted with cleaner air to get average mixing ratios. LP-DOAS I_2 observations can be explained with current chemistry schemes, if the I_2 source term is strong and within a few metres of the LP-DOAS lightpath. However the observations are better matched by the model using a recycling reaction to convert $IONO_2$ back into I_2.

Targeted observations should be able to distinguish between these two scenarios. During I_2 bursts in the polluted marine environment, it would be expected that localised increases in I_2 and IO, coupled with decreases in the $NO:NO_2$ ratio and growth of non-seasalt aerosol volumes would occur. If Reaction (1) is atmospherically important,

NO_3 and NO_2 mixing ratios would markedly increase, while NO_x and NO_y would not change greatly. If recycling does not play an atmospheric role then a small increase in NO_3, accompanied by a drop in NO_2 and NO_x and a substantial increase in NO_y (mainly attributable to an increase in $IONO_2$) should be observed. At the same time a substantial, and measurable, increase in nitrate fraction, and greater increase in mass loading, of the non-seasalt aerosol mode would occur.

LP-DOAS BrO measurements are higher than could be explained purely with a sea-salt bromine source. Unknown, extremely localised, emissions of reactive bromine could be the source for these measurements.

Supplementary material related to this article is available online at:
http://www.atmos-chem-phys-discuss.net/10/19429/2010/
acpd-10-19429-2010-supplement.zip.

References

Allan, B. J., McFiggans, G. B., Plane, J. M. C., and Coe, H.: Observations of iodine monoxide in the remote boundary layer, J. Geophys. Res., 105, 14363–14369, 2000. 19430

ApSimon, H. M., Barker, B. M., and Kayin, S.: Modelling studies of the atmospheric release and transport of ammonia in anticyclonic episodes, Atmos. Environ., 28, 665–678, 1994. 19436

Ball, S. M., Hollingsworth, A. M., Humbles, J., Leblanc, C., Potin, P., and McFiggans, G.: Spectroscopic studies of molecular iodine emitted into the gas phase by seaweed, Atmos. Chem. Phys., 10, 6237–6254, doi:10.5194/acp-10-6237-2010, 2010. 19432

Bloss, W. J., Lee, J. D., Johnson, G. P., Sommariva, R., Heard, D. E., Saiz-Lopez, A., Plane, J. M. C., McFiggans, G., Coe, H., Flynn, M., Williams, P., Rickard, A. R., and Fleming, Z. L.: Impact of halogen monoxide chemistry upon boundary layer OH and HO_2 con-

Multi-phase chemistry

D. Lowe et al.

Title Page

Abstract	Introduction
Conclusions	References
Tables	Figures

Back | Close

Full Screen / Esc

Printer-friendly Version

Interactive Discussion

centrations at a coastal site, Geophys. Res. Lett., 32, L06814, doi:10.1029/2004GL022084, 2005. 19430

Carpenter, L. J., Sturges, W. T., Penkett, S. A., Liss, P. S., Alicke, B., Heibestreit, K., and Platt, U.: Short-lived alkyl iodides and bromides at Mace Head, Ireland: links to biogenic sources and halogen oxide production, J. Geophys. Res., 104, 1679–1689, 1999. 19431

Davis, D., Crawford, J., Liu, S., McKeen, S., Bandy, A., Thornton, D., Rowland, F., and Blake, D.: Potential impact of iodine on tropospheric levels of ozone and other critical oxidants, J. Geophys. Res., 101, 2135–2147, 1996. 19430

Edwards, G. D. and Monks, P. S.: Performance of a single-monochromator diode array spectroradiometer for the determination of actinic flux and atmospheric photolysis frequencies, J. Geophys. Res., 108, 8546, doi:10.1029/2002JD002844, 2003. 19434

Gong, S. L.: A parameterization of sea-salt aerosol source function for sub- and super-micron particles, Global Biogeochem. Cy., 17, 1097, doi:10.1029/2003GB002079, 2003. 19435

Hoffmann, T., O'Dowd, C. D., and Seinfeld, J. H.: Iodine oxide homogeneous nucleation: An explanation for coastal new particle formation, Geophys. Res. Lett., 28, 1949–1952, 2001. 19430

Hoppel, W. A., Caffrey, P., and Frick, G. M.: Addition of Vertical Velocity to a One-Dimensional Aerosol and Trace Gas Model, Naval Research Laboratory, Washington DC, NRL/MR/7228–05-8852, 2005. 19435

Kaltsoyannis, N. and Plane, J. M. C.: Quantum chemical calculations on a selection of iodine-containing species (IO, OIO, INO_3, $(IO)_2$, I_2O_3, I_2O_4 and I_2O_5) of importance in the atmosphere, Phys. Chem. Chem. Phys., 10, 1723–1733, doi:10.1039/b715687c, 2008. 19432

Leigh, R. J., Ball, S. M., Whitehead, J., Leblanc, C., Shillings, A. J. L., Mahajan, A. S., Oetjen, H., Dorsey, J. R., Gallagher, M., Jones, R. L., Plane, J. M. C., Potin, P., and McFiggans, G.: Measurements and modelling of molecular iodine emissions, transport and photodestruction in the coastal region around Roscoff, Atmos. Chem. Phys. Discuss., 9, 21165–21198, doi:10.5194/acpd-9-21165-2009, 2009. 19432, 19438, 19439

Lowe, D., Topping, D., and McFiggans, G.: Modelling multi-phase halogen chemistry in the remote marine boundary layer: investigation of the influence of aerosol size resolution on predicted gas- and condensed-phase chemistry, Atmos. Chem. Phys., 9, 4559–4573, doi:10.5194/acp-9-4559-2009, 2009. 19434

Mahajan, A. S., Oetjen, H., Lee, J. D., Saiz-Lopez, A., McFiggans, G. B., and Plane, J. M.: High bromine oxide concentrations in the semi-polluted boundary layer, Atmos. Environ., 43,

3811–3818, doi:10.1016/j.atmosenv.2009.05.033, 2009a. 19431, 19432, 19433, 19444

Mahajan, A. S., Oetjen, H., Saiz-Lopez, A., Lee, J. D., McFiggans, G. B., and Plane, J. M. C.: Reactive iodine species in a semi-polluted environment, Geophys. Res. Lett., 36, L16803, doi:10.1029/2009GL038018, 2009b. 19431, 19432, 19442, 19443

McFiggans, G., Plane, J. M. C., Allan, B. J., Carpenter, L. J., Coe, H., and O'Dowd, C.: A modeling study of iodine chemistry in the marine boundary layer, J. Geophys. Res., 105, 14371–14385, 2000. 19430

McFiggans, G., Coe, H., Burgess, R., Allan, J., Cubison, M., Alfarra, M. R., Saunders, R., Saiz-Lopez, A., Plane, J. M. C., Wevill, D., Carpenter, L., Rickard, A. R., and Monks, P. S.: Direct evidence for coastal iodine particles from Laminaria macroalgae – linkage to emissions of molecular iodine, Atmos. Chem. Phys., 4, 701–713, doi:10.5194/acp-4-701-2004, 2004. 19430

McFiggans, G., Bale, C. S. E., Ball, S. M., Beames, J. M., Bloss, W. J., Carpenter, L. J., Dorsey, J., Dunk, R., Flynn, M. J., Furneaux, K. L., Gallagher, M. W., Heard, D. E., Hollingsworth, A. M., Hornsby, K., Ingham, T., Jones, C. E., Jones, R. L., Kramer, L. J., Langridge, J. M., Leblanc, C., LeCrane, J.-P., Lee, J. D., Leigh, R. J., Longley, I., Mahajan, A. S., Monks, P. S., Oetjen, H., Orr-Ewing, A. J., Plane, J. M. C., Potin, P., Shillings, A. J. L., Thomas, F., von Glasow, R., Wada, R., Whalley, L. K., and Whitehead, J. D.: Iodine-mediated coastal particle formation: an overview of the Reactive Halogens in the Marine Boundary Layer (RHaMBLe) Roscoff coastal study, Atmos. Chem. Phys., 10, 2975–2999, doi:10.5194/acp-10-2975-2010, 2010. 19431

Monahan, E. C., Spiel, D. E., and Davidson, K. L.: A model of marine aerosol generation via whitecaps and wave disruption, in: Oceanic Whitecaps, edited by: Monahan, E. C. and Niocaill, G. M., 167–174, D. Reidel, Norwell, Mass., 1986. 19435

Myrup, L. O. and Ranzieri, A. J.: A Consistent Scheme for Estimating Diffusivities to Be Used in Air Quality Models, Tech. Rep. CA-DOT-TL-7169-3-76-32, California Department of Transportation, 1976. 19436

O'Dowd, C. D., Smith, M. H., Conserdine, I. E., and Lowe, J. A.: Marine aerosol, sea salt, and the marine sulphur cycle: a short review, Atmos. Environ., 31, 73–80, 1997. 19435

O'Dowd, C. D., Jimenez, J. L., Bahreini, R., Flagan, R. C., Seinfeld, J. H., Hameri, K., Pirjola, L., Kulmala, M., and Jennings, S. G.: Marine aerosol formation from biogenic emissions, Nature, 417, 632–636, 2002. 19430

Palmer, C. J., Anders, T. L., Carpenter, L. J., Kpper, F. C., and McFiggans, G.: Iodine and

Multi-phase chemistry

D. Lowe et al.

Title Page

Abstract	Introduction
Conclusions	References
Tables	Figures

Back | Close

Full Screen / Esc

Printer-friendly Version

Interactive Discussion

halocarbon response of Laminaria digitata to oxidative stress and links to atmospheric new particle production, Environ. Chem., 2, 282–290, 2005. 19431

Pechtl, S., Lovejoy, E. R., Burkholder, J. B., and von Glasow, R.: Modeling the possible role of iodine oxides in atmospheric new particle formation, Atmos. Chem. Phys., 6, 505–523, doi:10.5194/acp-6-505-2006, 2006. 19434

Peters, C., Pechtl, S., Stutz, J., Hebestreit, K., Hönninger, G., Heumann, K. G., Schwarz, A., Winterlik, J., and Platt, U.: Reactive and organic halogen species in three different European coastal environments, Atmos. Chem. Phys., 5, 3357–3375, doi:10.5194/acp-5-3357-2005, 2005. 19431

Platt, U. and Hönninger, G.: The role of halogen species in the troposphere, Chemosphere, 51, 325–338, 2003. 19430

Porter, J. N. and Clarke, A. D.: Aerosol size distribution models based on in situ measurements, J. Geophys. Res., 102, 6035–6045, 1997. 19437

Press, W. H., Flannery, B. P., Teukolsky, S. A., and Vetterling, W. T.: Numerical Recipes (FOR-TRAN Version), Cambridge University Press, Cambridge, 1989. 19436

PPyles, R. D., Weare, B. C., Paw U, K. T., and Gustafson, W.: Coupling between the University of California, Davis, Advanced Canopy-Atmosphere-Soil Algorithm (ACASA) and MM5: preliminary results for July 1998 for Western North America, J. Appl. Meterol., 42, 557–569, 2003. 19436

Pyles, R. D., Paw U, K. T., and Falk, M.: Directional wind shear within an old-growth temperate rainforest: observations and model results, Agr. Forest Meteorol., 125, 19–31, doi:10.1016/j.agrformet.2004.03.007, 2004. 19436

Read, K. A., Mahajan, A. S., Carpenter, L. J., Evans, M. J., Faria, B. V. E., Heard, D. E., Hopkins, J. R., Lee, J. D., Moller, S. J., Lewis, A. C., Mendes, L., McQuaid, J. B., Oetjen, H., Saiz-Lopez, A., Pilling, M. J., and Plane, J. M. C.: Extensive halogen-mediated ozone destruction over the Tropical Atlantic Ocean., Nature, 453, 1232–1235, doi:10.1038/nature07035, 2008. 19430

Saiz-Lopez, A. and Plane, J. M. C.: Novel iodine chemistry in the marine boundary layer, Geophys. Res. Lett., 31, L04112, doi:10.1029/2003GL019215, 2004. 19431

Saiz-Lopez, A., Plane, J. M. C., and Shillito, J. A.: Bromine oxide in the mid-latitude marine boundary layer, Geophys. Res. Lett., 31, L03111, doi:10.1029/2003GL018956, 2004. 19431

Saiz-Lopez, A., Plane, J. M. C., Mahajan, A. S., Anderson, P. S., Bauguitte, S. J.-B., Jones, A. E., Roscoe, H. K., Salmon, R. A., Bloss, W. J., Lee, J. D., and Heard, D. E.:

Multi-phase chemistry

D. Lowe et al.

Title Page

Abstract | Introduction

Conclusions | References

Tables | Figures

◀ | ▶

◀ | ▶

Back | Close

Full Screen / Esc

Printer-friendly Version

Interactive Discussion

On the vertical distribution of boundary layer halogens over coastal Antarctica: implications for O_3, HO_x, NO_x and the Hg lifetime, Atmos. Chem. Phys., 8, 887–900, doi:10.5194/acp-8-887-2008, 2008. 19434, 19451

Sander, R., Keene, W. C., Pszenny, A. A. P., Arimoto, R., Ayers, G. P., Baboukas, E., Cainey, J. M., Crutzen, P. J., Duce, R. A., Hönninger, G., Huebert, B. J., Maenhaut, W., Mihalopoulos, N., Turekian, V. C., and Van Dingenen, R.: Inorganic bromine in the marine boundary layer: a critical review, Atmos. Chem. Phys., 3, 1301–1336, doi:10.5194/acp-3-1301-2003, 2003. 19431

Slinn, S. A. and Slinn, W. G. N.: Predictions for particle deposition on natural waters, Atmos. Environ., 14, 1013–1016, 1980. 19435

Topping, D., Lowe, D., and McFiggans, G.: Partial Derivative Fitted Taylor Expansion: An efficient method for calculating gas-liquid equilibria in atmospheric aerosol particles: 1. Inorganic compounds, J. Geophys. Res., 114, D04304, doi:10.1029/2008JD010099, 2009. 19434

Toyota, K., Takahashi, M., and Akimoto, H.: Modeling multi-phase halogen chemistry in the marine boundary layer with size-segregated aerosol module: implications for quasi-size-dependent approach, Geophys. Res. Lett., 28, 2899–2902, doi:10.1029/2001GL012916, 2001. 19437

Vogt, R., Crutzen, P. J., and Sander, R.: A mechanism for halogen release from sea-salt aerosol in the remote marine boundary layer, Nature, 383, 327–330, 1996. 19431

Wada, R., Beames, J. M., and Orr-Ewing, A. J.: Measurement of IO radical concentrations in the marine boundary layer using a cavity ring-down spectrometer, J. Atmos. Chem., 58, 69–87, doi:10.1007/s10874-007-9080-z, 2007. 19431

Whalley, L. K., Furneaux, K. L., Gravestock, T., Atkinson, H. M., Bale, C. S. E., Ingham, T., Bloss, W. J., and Heard, D. E.: Detection of iodine monoxide radicals in the marine boundary layer using laser induced fluorescence spectroscopy, J. Atmos. Chem., 58, 19–39, 2007. 19431
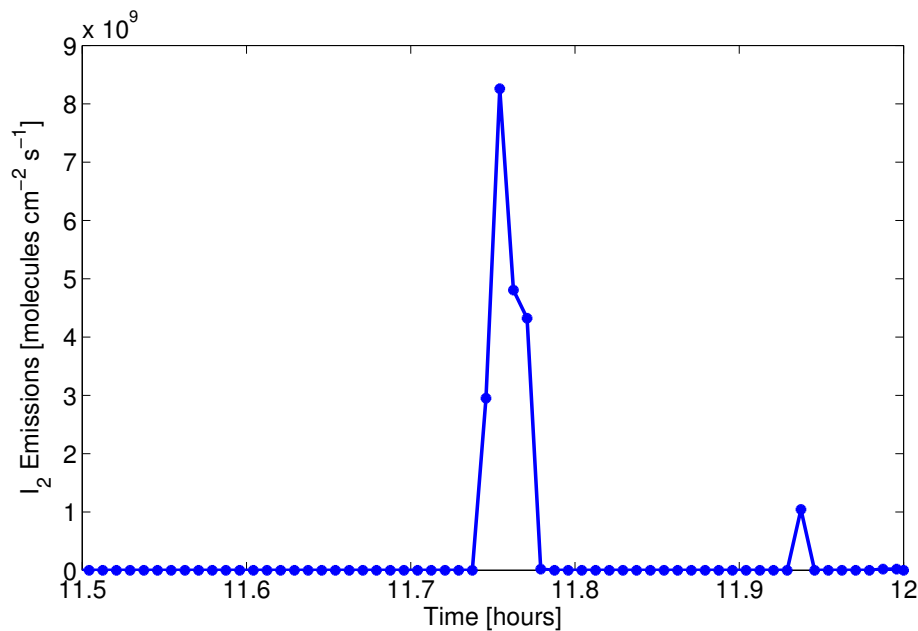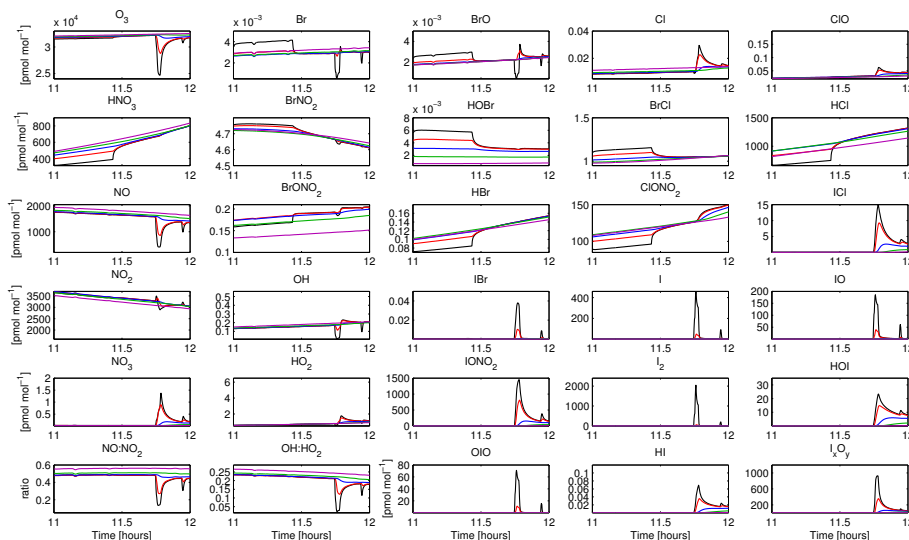
Title Page

Abstract | Introduction

Conclusions | References

Tables | Figures

|◄ | ►|

◄ | ►

Back | Close

Full Screen / Esc

Printer-friendly Version

Interactive Discussion

Table 1. I_xO_y chemistry from Saiz-Lopez et al. (2008).

Reaction	Rate
$IO+OIO=I_2O_3$	1.5×10^{-10}
$OIO+OIO=I_2O_4$	1.0×10^{-10}
$I_2O_2+O_3=I_2O_3+O_2$	1.0×10^{-12}
$I_2O_3+O_3=I_2O_4+O_2$	1.0×10^{-12}
$I_2O_4+O_3=I_2O_5+O_2$	1.0×10^{-12}

Table 2. Initial gas-phase chemical mixing ratios (given in $\mathrm{pmol\,mol^{-1}}$).

Species	mixing ratio
NO_2	20
HCHO	300
PAN	10
CO	70 000
HNO_3	10
SO_2	90
DMS	60
H_2O_2	600
C_2H_6	500
HCl	40
CH_3I	2
C_3H_7I	1
NH_3	80
O_3	40 000

Table 3. Gas-phase source terms, in molecules cm^{-2}. The Sea terms are used for the Atlantic and Channel legs of the model run (and for the sea-section of the Roscoff leg). The Land terms are used for the UK leg of the model run – the NO_x term is split between NO and NO_2 based on the $NO:NO_2$ of the lowest level of the model column at that point in time.

Species	source term
Sea	
NO	2×10^8
NH_3	4×10^8
DMS	2×10^9
CH_3I	6×10^6
C_3H_7I	1×10^7
CH_2ClI	2×10^7
CH_2I_2	3×10^7
CH_2BrI	2×10^7
Land	
NO_x	5×10^{11}
NH_3	1×10^{11}
SO_2	1×10^{11}
CO	2×10^{12}

Table 4. Gas-phase loss velocities, $v_{d,g}$, in $\mathrm{cm\,s^{-1}}$. Representing deposition at base of model column.

Species	$v_{d,g}$
O_3	0.04
H_2O_2	0.5
NO_2	0.1
N_2O_5	1.0
HNO_3	2.0
NH_3	0.1
$HCHO$	0.5
$HCOOH$	1.0
HCl	2.0
$HOCl$	1.0
$ClNO_3$	1.0
HBr	2.0
$HOBr$	1.0
$BrNO_3$	1.0
CH_3SOCH_3	1.0
SO_2	0.5
H_2SO_4	1.0
CH_3SO_3H	1.0
HI	1.0
HOI	1.0
INO_3	1.0
INO_2	1.0

Table 5. Parameters for the non-seasalt aerosol distribution used in study. N_{tot} is in cm^{-3} and R_N in µm. The log-normal particle size distribution is calculated according to $\frac{dN(r)}{dr} = \frac{N_{tot}}{\ln\sigma\sqrt{2\pi}} \times \exp\left(-\frac{(\ln r - \ln R_N)^2}{2(\ln\sigma)^2}\right)$.

Mode	N_{tot}	R_N	σ
non-seasalt	300	0.088	1.29
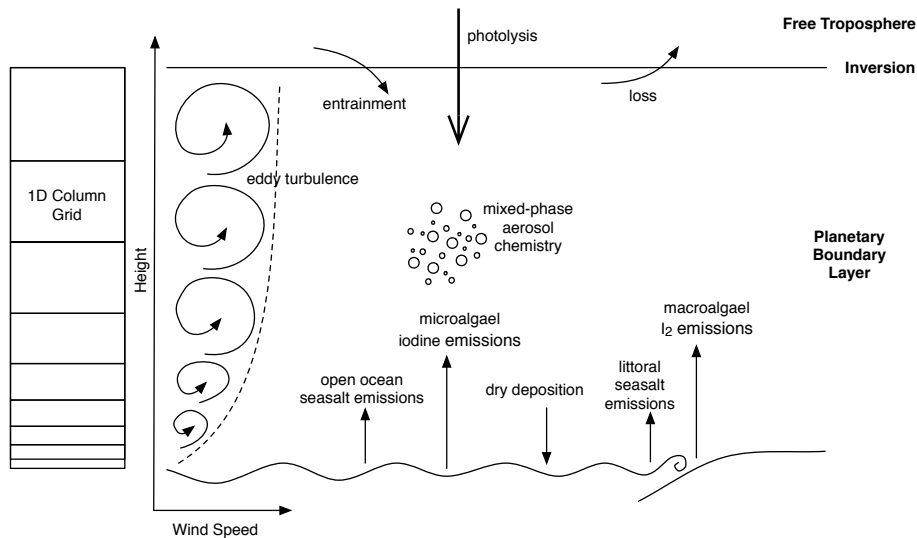
Fig. 1. Schematic of the major processes dealt with in MANIC-1D. An example, non-linear, vertical grid is shown on the left.

Fig. 2. I_2 emissions used for the "low tide" scenario. Calculated using a back trajectory from the Roscoff measurement site at 12:30 p.m. on 10 September 2006.

Fig. 3. Mixing ratios of major gas-phase chemical species at different levels through the model column for the base case, low tide, model run. Black, red, blue, green, and purple lines represent mixing ratios at heights of 0.5, 8, 60, 250 and 650 m.
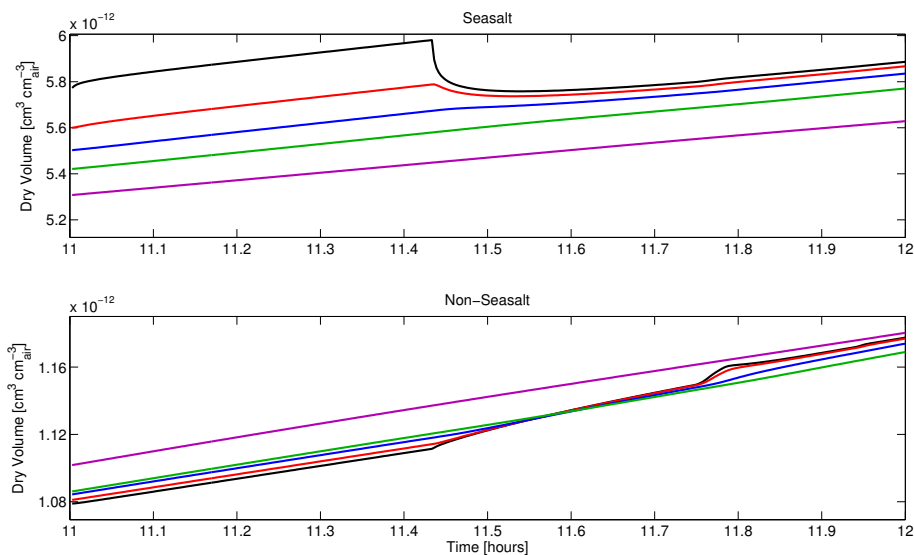
Fig. 4. Total dry volume for the seasalt and non-seasalt modes at different levels through the model column for the base case, low tide, model run. Black, red, blue, green, and purple lines represent mixing ratios at heights of 0.5, 8, 60, 250 and 650 m.
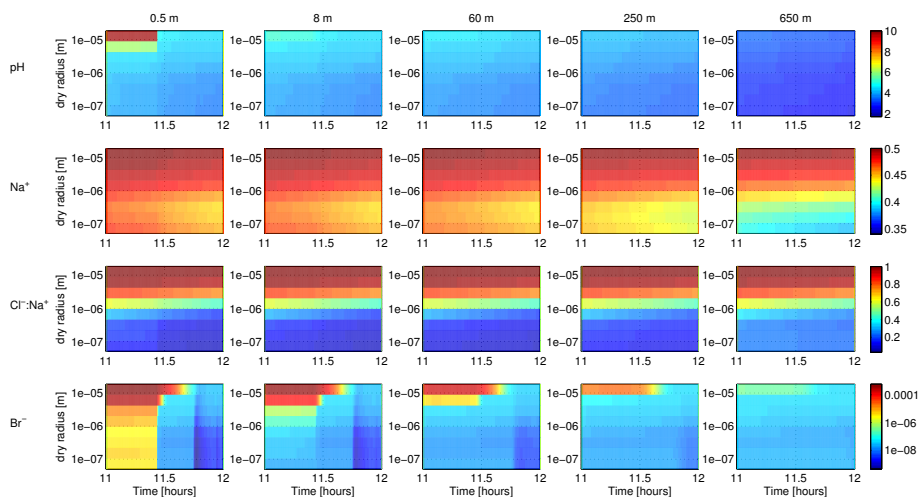
Fig. 5. Seasalt compositional data at different levels through the model column for the base case, low tide, model run. First row is pH. Second and fourth rows are Na^+ and Br^- dry mole fractions, respectively. The third row is the ratio of Cl^- and Na^+ dry mole fractions.
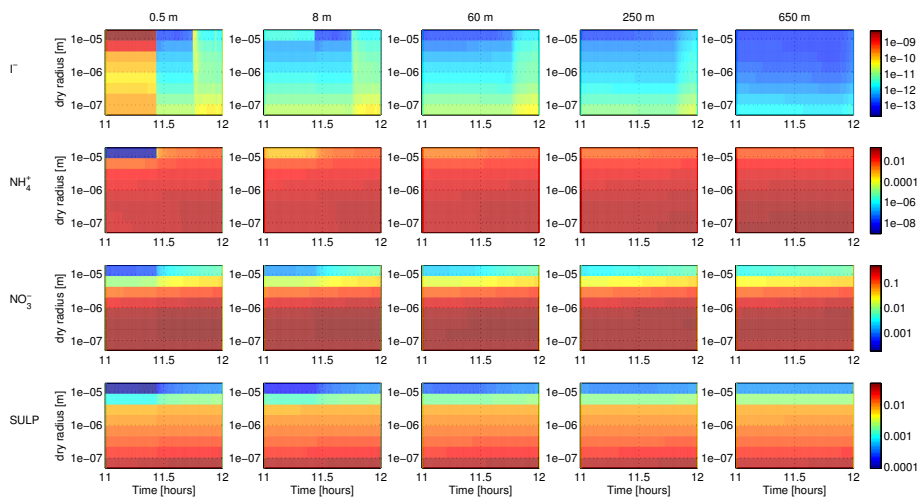
Fig. 6. Seasalt compositional data at different levels through the model column for the base case, low tide, model run. First, second and third rows are I^-, NH_4^+ and NO_3^- dry mole fractions, respectively. The fourth row is the summed dry mole fraction of $H_2SO_{4(aq)}$, HSO_4^- and SO_4^{2-}.
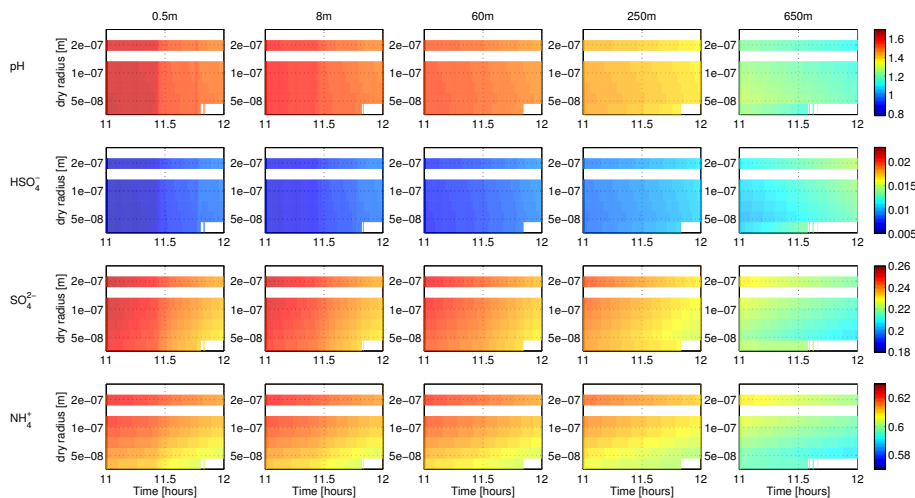
Fig. 7. Non-seasalt compositional data at different levels through the model column for the base case, low tide, model run. First row is pH. Second, third and fourth rows are HSO_4^-, SO_4^{2-} and NH_4^+ dry mole fractions, respectively.
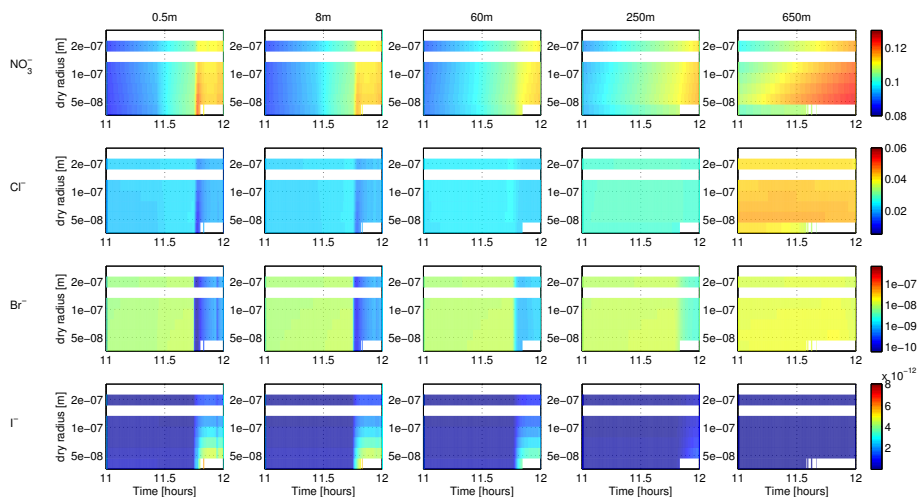
Fig. 8. Non-seasalt compositional data at different levels through the model column for the base case, low tide, model run. First, second, third and fourth rows are NO_3^-, Cl^-, Br^- and I^- dry mole fractions, respectively.

Fig. 9. Mixing ratios of I_2, IO, OIO, I_xO_y, NO_3, and ratio of I_2:IO, in the lowest five layers of the model column for the base case, low tide, model run. Black, red, blue, green, and purple lines represent levels with their centres at 0.5, 2, 4.5, 8 and 12.5 m, respectively.

Fig. 10. Mixing ratios of I_2, IO, OIO, I_xO_y, NO_3, and ratio of I_2:IO, in the lowest five layers of the model column for the I_2 recycling, low tide, model run. Black, red, blue, green, and purple lines represent levels with their centres at 0.5, 2, 4.5, 8 and 12.5 m, respectively.
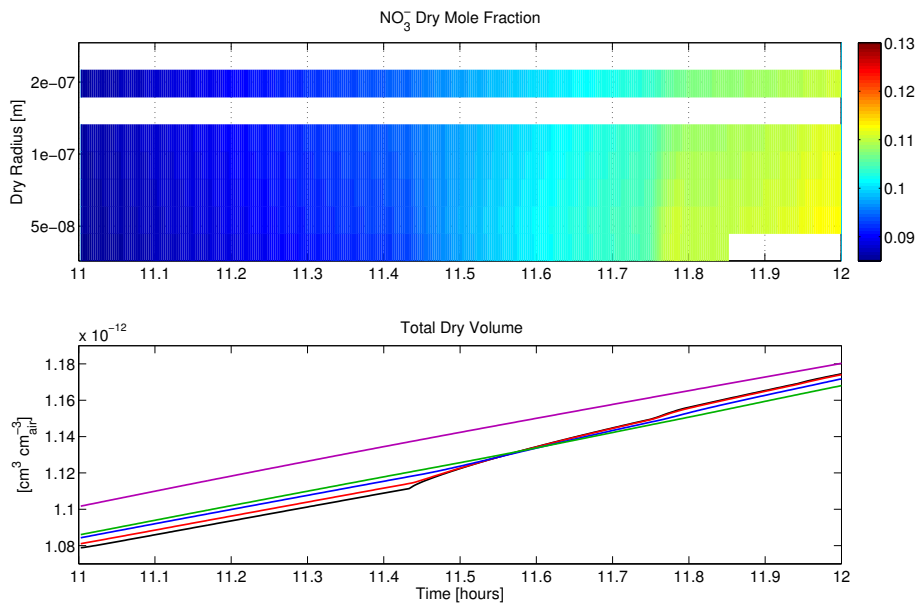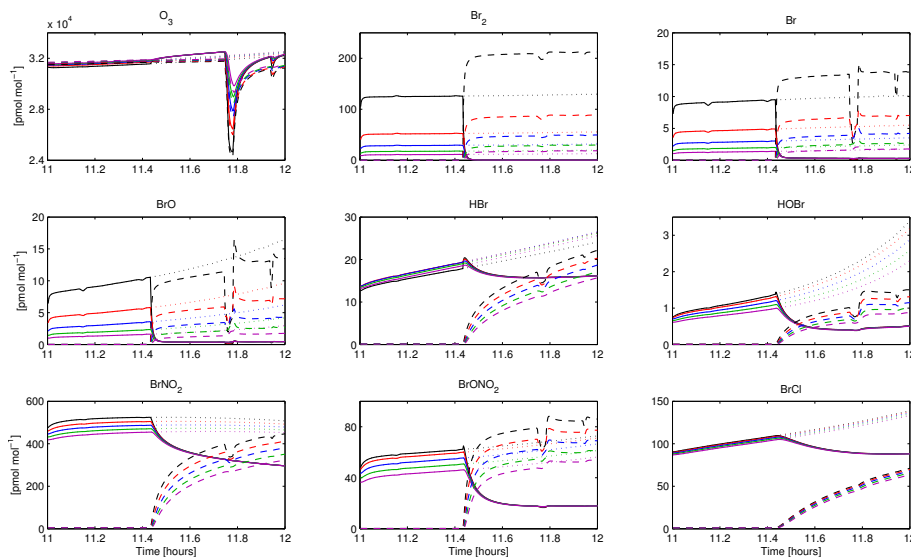
Fig. 11. Non-seasalt aerosol properties for the I_2 recycling, low tide, model run. Top panel is the dry mole fraction of NO_3^- at a height of 0.5 m. Bottom panel is total dry volume of the non-seasalt mode at heights of 0.5, 8, 60, 250 and 650 m (black, red, blue, green, and purple lines, respectively).

Fig. 12. Mixing ratios of O_3 and the major bromine compounds, in the lowest five layers of the model column. Black, red, blue, green, and purple lines represent levels with their centres at 0.5, 2, 4.5, 8 and 12.5 m, respectively. Solid and dotted lines represent mixing ratios from the model runs with a sea based Br_2 source (solid lines are for the low-tide scenario, dotted lines for the high-tide scenario). Dashed lines represent mixing ratios from the low-tide model run with a beach based Br_2 source.